# Ionospheric energy input in response to changes in solar wind driving: Statistics from the SuperDARN and AMPERE campaigns

**D. D. Billett[1], K. A. McWilliams[1], G. W. Perry[2], L. B. N. Clausen[3], B. J. Anderson[4]**

[1]Institute of Space and Atmospheric Studies, University of Saskatchewan, Saskatoon, SK, Canada
[2]Center for Solar-Terrestrial Research, New Jersey Institute of Technology, Newark, NJ, USA
[3]Department of Physics, University of Oslo, Oslo, Norway
[4]Applied Physics Laboratory, Johns Hopkins University, Laurel, Maryland, USA

**Key Points:**

- SuperDARN and AMPERE derived Poynting flux distributions are generated with a two-minute resolution.
- A superposed epoch analysis is performed for transitions of the IMF $B_z$ component.
- There is spatial and temporal asymmetry to how the Poynting flux morphology responds to opposite $B_z$ transitions.

Corresponding author: D. D. Billett, daniel.billett@usask.ca

## Abstract

For over a decade, the Super Dual Auroral Radar Network (SuperDARN) and the Active Magnetosphere and Planetary Electrodynamics Response Experiment (AMPERE) have been measuring ionospheric convection and field-aligned currents in the high-latitude regions, respectively. Using both, whole hemisphere maps of the magnetosphere-ionosphere energy transfer rate (the Poynting flux) have been generated with a time resolution of two minutes between 2010 and 2017. These uniquely data driven Poynting flux patterns are used in this study to perform a superposed epoch analysis of the northern hemisphere ionospheric response to transitions of the IMF $B_z$ component. We discuss the difference in the distribution of Poynting flux between the magnetosphere-ionosphere Dungey cycle "switching on" and "switching off" to solar wind driving, revealing that they are not symmetric temporally or spatially.



## Plain Language Summary

The Earth's high-latitude upper atmosphere (the ionosphere, upwards of 100km in altitude) is consistently bombarded with solar energy that takes the form of electric currents aligned with Earth's magnetic field. The magnetosphere has two generalised states, "open" and "closed". Open is when the Earth and solar magnetic fields connect to each other on the dayside, allowing energy into the atmosphere from the solar wind. Closed is when the fields do not connect (or do not connect simply) and thus not as much energy enters the atmosphere. The open or closed criteria depends on the direction of the solar magnetic field, which varies constantly. In this study, we utilise nearly 8 years of data to generate average patterns of ionospheric energy input at various intervals before and after the solar-magnetosphere system transitions from open to closed, and vice versa. We discuss the spatial and temporal timescales upon which the energy varies in response to the relatively symmetric transitions, finding that they do not result in symmetric changes in the ionospheric energy input patterns.


## 1 Introduction

In 2009, the Iridium constellation of satellites began consistently delivering magnetic field data at their orbital altitude of ∼780 km to be processed as part of the Active Magnetosphere and Planetary Electrodynamics Response Experiment (AMPERE; Anderson et al., 2014). AMPERE has allowed for the derivation of global-scale pertur-

bation magnetic fields at F-region ionospheric altitudes (at a typical 10-minute resolution), which are subsequently processed into patterns of the high-latitude field-aligned currents (FACs). Overlapping with the entirety of the AMPERE dataset from its inception to the present day has been consistent measurements of ionospheric plasma flows from the Super Dual Auroral Radar Network (SuperDARN; Greenwald et al., 1995). As of 2021, the SuperDARN consists of 36 high-frequency radars in both the northern and southern hemispheres that are used conjunctively to generate instantaneous patterns of the high-latitude ionospheric convection pattern (Chisham et al., 2007; Nishitani et al., 2019), at a two-minute resolution.

SuperDARN derived convection, or electric potential ($\Phi$), patterns can be converted to the electric field ($\mathbf{E}$) via the relation $\mathbf{E} = -\nabla\Phi$. AMPERE derived perturbation magnetic fields ($\delta\mathbf{B}$), based on the assumption that the magnetic field is near-vertical at high latitudes, can then be used in conjunction with $\mathbf{E}$ to calculate the total energy transferred between the magnetosphere and ionosphere through field aligned currents (FACs), the Poynting flux ($\mathbf{S}_{||}$), using Poynting's theorem:

$$\mathbf{S}_{||} = -\frac{1}{\mu_0}\left(\mathbf{E} \times \delta\mathbf{B}\right) \cdot \hat{\mathbf{r}} \tag{1}$$

where $\hat{\mathbf{r}}$ is the unit vector parallel to the geomagnetic field and $\mu_0$ is the permeability of free space. Previously, a dataset of Poynting flux patterns for the northern hemisphere ionosphere has been generated for the entire overlapping AMPERE-SuperDARN datasets between 2010 and 2017 using Equation 1, which have been shown to be consistent with several models and observations (Billett et al., 2021).

This study utilises the new dataset of northern hemisphere Poynting flux maps to examine its statistical response to changes in solar wind driving conditions, primarily after sustained transitions of the Interplanetary Magnetic Field (IMF) $B_z$ component in Geocentric Solar Magnetospheric (GSM) coordinates. These types of IMF transitions are akin to "switching on" ($B_z > 0$ to $B_z < 0$) and "switching off" ($B_z < 0$ to $B_z > 0$) magnetospheric driving of the ionosphere via reconnection at the magnetopause, inducing the Earth's Dungey cycle (Dungey, 1961; Cowley & Lockwood, 1992). Although this is a simplistic view of magnetosphere-ionosphere coupling given that magnetopause reconnection can still occur at the magnetopause when the IMF $B_z$ is positive (Onsager et al., 2001), whether the IMF vector is southward ($B_z < 0$) or northward ($B_z > 0$)

orientated is the most significant indicator of magnetospheric energy input into the ionosphere (Milan, 2009).

The "switching on" of the magnetosphere-ionosphere driving system (i.e., a positive-to-negative IMF $B_z$ transition) has been extensively studied. For example, the ionospheric electric field is known to respond dynamically to changes in the near-Earth solar wind on the order of minutes (e.g. Murr & Hughes, 2001; Yu & Ridley, 2009; Snekvik et al., 2017). This response begins on the dayside and progresses to the nightside, with the ionospheric electric field fully reconfiguring to a negative $B_z$ orientation within tens of minutes (e.g. Murr & Hughes, 2001; Dods et al., 2017). The global FACs system finish developing much later, on the order of hours (Coxon et al., 2019). Ionospheric conductivity is also known to play an important role in the rate of FAC formation, contributing to seasonal asymmetries (Coxon et al., 2016).

Negative to positive turnings of the IMF $B_z$ have less commonly been studied. Lobe reconnection under positive $B_z$ results in the development of a new FAC system (NBZ; Iijima et al., 1984), thus lowering the decay rate of the total dayside current and bringing it more in line with the total nightside current decay (Milan et al., 2018). Decay rates are further complicated by the different responses of reconnection driven magnetospheric convection and viscous interaction or flywheel driven convection under positive $B_z$ (Bhattarai et al., 2012). Low nightside conductance may in fact result in faster nightside FAC decay due to weaker line-tying of magnetic field lines (Moretto et al., 2018, 2021).

In this paper, we present the response of the northern hemispheric Poynting flux to the aforementioned $B_z$ transitions as a superposed epoch analysis. We discuss how the overlapping SuperDARN and AMPERE data sets were used to do this in section 2. Results are shown in section 3, whilst we discuss the differences in how Poynting flux increases or decreases depending on the $B_z$ transition in section 4.

## 2 Data processing

Maps of the high-latitude Poynting flux were generated for each overlapping AMPERE $\delta\mathbf{B}$ map and SuperDARN convection pattern in the northern hemisphere using the method described by Waters et al. (2004). In short, both $\delta\mathbf{B}$ from AMPERE and $\mathbf{E}$ from the SuperDARN are placed into an equal area (∼200x400 km) grid poleward of 60° AACGM (Shepherd, 2014) latitude which is also fixed in local time, where each cell

is 2° of latitude tall. Equation 1 is then used to derive the Poynting flux on the same grid. All latitudes and magnetic local times (MLTs) mentioned henceforth are referring to AACGM latitude and local time, respectively.

As the global SuperDARN convection patterns are spherical harmonic fits to the plasma velocity data from individual radars (Ruohoniemi & Baker, 1998), a threshold of 200 gridded SuperDARN line-of-sight velocity data points per pattern is imposed before using them to calculate the Poynting flux. This ensures there is generally a good spread of real radar velocity data across most local times for any given convection map and reduces the amount of "usable" SuperDARN convection patterns for Poynting flux measurements by around 55% (Billett et al., 2018). The SuperDARN radar data is also filtered so that E-region ionospheric backscatter is removed, giving the convection patterns an assumed F-region altitude of approximately 250 km. Convection patterns use SuperDARN data integrated over two minutes.

The AMPERE data is assumed to be from an altitude of 780 km, which is subsequently scaled to an altitude of 250 km to match the SuperDARN data. This is done using the 3/2 relationship described by Knipp et al. (2014) and results in $\delta\mathbf{B}$ being approximately 1.12 times larger than measured. $\delta\mathbf{B}$ maps have a two-minute resolution and a sliding 10-minute integration window, so when combined with SuperDARN data, Poynting flux maps are calculated at a two-minutes resolution.

In this study, a superposed epoch analysis of the Poynting flux with an epoch spacing of two minutes was carried out for sustained transitions of the IMF $B_z$ component. IMF data is obtained from the 1-minute resolution OMNI dataset (retrieved from `http://omniweb.gsfc.nasa.gov`) and is time shifted forward by 10 minutes to account for the travel between the magnetopause and ionosphere. "Sustained" transitions are defined as intervals where $B_z$ was constantly northward (southward) orientated for at least 30 minutes prior to becoming southward (northward), upon which the sign of $B_z$ remained the same for an additional 30 minutes. Using 30 minutes prior to the transition allows time for the ionosphere to be "settled" under the initial negative or positive $B_z$ by epoch $t_0$. 30 minutes after the transition gives a window to examine the Poynting flux response to the IMF change, which is long enough for the ionospheric electric field to converge to state equivalent to statistical patterns on average (Grocott & Milan, 2014). In order to

maintain a high number of Poynting flux maps for averaging, no $B_z$ magnitude threshold was imposed and the IMF $B_y$ component was not considered.

## 3 Results

The results of the Poynting flux superposed epoch analysis, for sustained north-to-south and south-to-north IMF $B_z$ transitions, are shown in Figure 1. There were 1301 north-to-south and 1307 south-to-north transitions during the SuperDARN-AMPERE overlap period, but only Poynting flux maps which met the 200 SuperDARN data point threshold were used in the average for each epoch (the total in each denoted by the number in the top left of the sub-plots). There was no transition bias towards a specific year, season, sign of $B_y$ or magnitude of $B_z$.

The patterns shown in Figure 1 are from 4 minutes prior to the IMF transition to 30 minutes after in two-minute intervals. Epochs prior to $t_0 - 4$ are not shown here as they do not vary significantly from $t_0 - 4$. Only positive (downward) Poynting fluxes are shown, as negative (upward) values are nearly always small, thus averaging out. This is to be expected because the ionosphere is on average a passive load to the magnetosphere, not vice versa. We note that more Poynting maps meet the 200 SuperDARN data point criteria when the IMF is southward, signifying the SuperDARN radars receiving more ionospheric backscatter during more geomagnetically active periods.

For the north-to-south transition in Figure 1a, there are regions of enhanced downward Poynting flux (PF) that are consistent in their morphology throughout all epochs. These are lower latitude enhancements around 70° latitude on both the dawn and dusk sides, as well as a higher latitude enhancement around 80° latitude centred slightly duskward of noon MLT. Before $t_0$, the highest PF magnitude is in the high-latitude dayside region. From $t_0$ to $t_0$+30, PF gradually increases starting at dayside local times and eventually affecting nightside local times. The largest PF magnitudes at $t_0$+30 are located around 80° latitude centred on noon MLT, as well as around 70° latitude in the 05-09 and 13-18 MLT regions. PF is noticeably smaller for nightside local times, and non-existent near midnight for all latitudes. There is a gradual movement of dawn and duskside enhanced PF equatorward between $t_0$ and $t_0$+30.

In Figure 1b, the IMF $B_z$ south-to-north transition of downward Poynting flux is shown. Before $t_0$, the magnitudes are similar to that in the $t_0$+30 epoch of the northward-

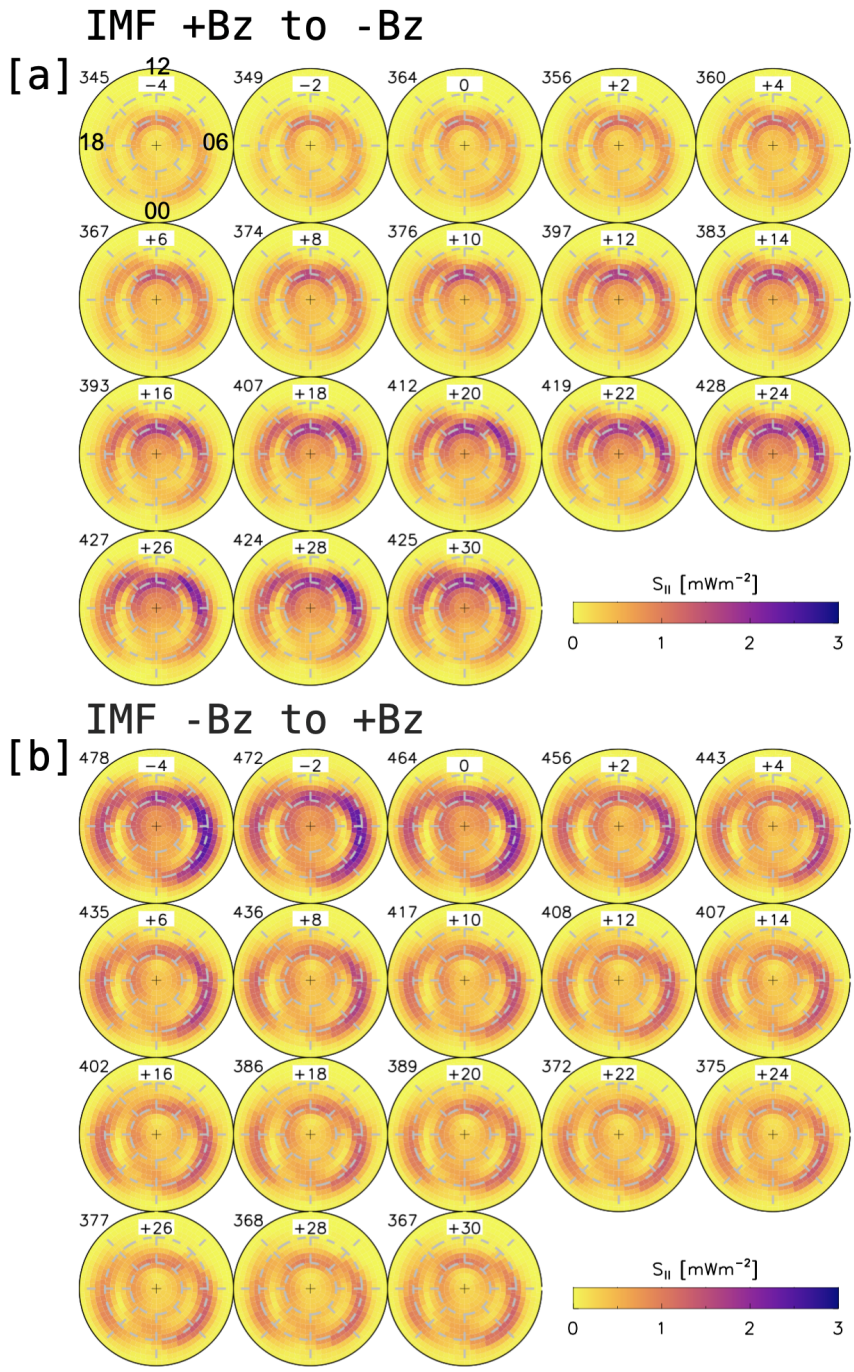


**Figure 1.** Superposed epoch maps of the downward Poynting flux from $t_0 - 4$ to $t_0 + 30$, for [a] northward-to-southward and [b] southward-to-northward IMF $B_z$ transitions. Plots are polar projections in AACGM latitude and local time. Noon is to the top and dawn is to the right of each plot. Concentric circles separate 10° of latitude, down to a 60° minimum. Numbers in the top left of each plot denote the number of averages in each epoch.

to-southward transition shown in 1a, but the enhanced dawnside PF extends significantly closer to midnight MLT. At +2 minutes, there appears to be a steep decrease in PF magnitude when compared to $t_0$, which is particularly evident in the high-latitude dayside and lower latitude dawnside regions. A similar sharp change after $t_0$ does not seem to be present for the $B_z$ northward-to-southward transition in Figure 1a. At $t_0$+30 in Figure 1b, the PF is decreased at all local times from $t_0$.

To further examine the changes in downward Poynting flux magnitudes after the IMF $B_z$ transitions, Figure 2 shows sets of time series plots from 30 minutes prior to 30 minutes after a transition. The data has been averaged over four local time sectors 6 hours in width each: the nightside (21-03 MLT, red diamonds), dawnside (03-09 MLT, blue squares), dayside (09-15 MLT, yellow circles) and duskside (15-21 MLT, green triangles). The time series have also been area integrated both below and above 75° latitude to differentiate between Poynting flux variations in the lower and higher latitude regions identified previously. The result is the total inbound power for 8 sectors, which we refer to as Poynting flux power (PFP).

Figure 2a shows the $B_z$ north-to-south transition for the lower latitude (<75°) region. Prior to $t_0$, dawnside and nightside PFP is the largest (∼0.3 GW), followed by duskside (∼0.25 GW) and dayside (<0.05 GW). Dawn and duskside PFP increase after $t_0$ at a steady rate, to 0.9 and 0.8 GW respectively at $t_0$+30, with duskside PFP overtaking the magnitude of nightside PFP. Dayside PFP increases to 0.2 GW after $t_0$, whilst nightside PFP changes very little.

For the higher latitude (<75°) $B_z$ north-to-south transition (Figure 2b), all regions average a PFP between 0.2 and 0.4 GW before $t_0$. Dayside PFP is largest and undergoes the most significant increase between $t_0$ and $t_0$+30, up to ∼ 1.1 GW. Dawn and duskside PFP remain comparable as they increase to 0.7 GW, while nightside PFP increases very gradually to 0.35 GW.

In Figure 2c, the $B_z$ south-to-north transition for the lower latitude region is shown. From before $t_0$ to $t_0$+30, dawnside PFP decreases from 1.4 to 0.6 GW, duskside from 1.05 to 0.5 GW, nightside from 0.6 to 0.5 GW and dayside from 0.35 to 0.1 GW. We note that the PFP magnitudes at the beginning ($t_0$-30) of the epoch analysis, in particular on the dawn and dusk sides, are larger than corresponding magnitudes at $t_0$+30 in figure 2a (i.e., the reverse $B_z$ transition). This implies that 30 minutes is not long enough

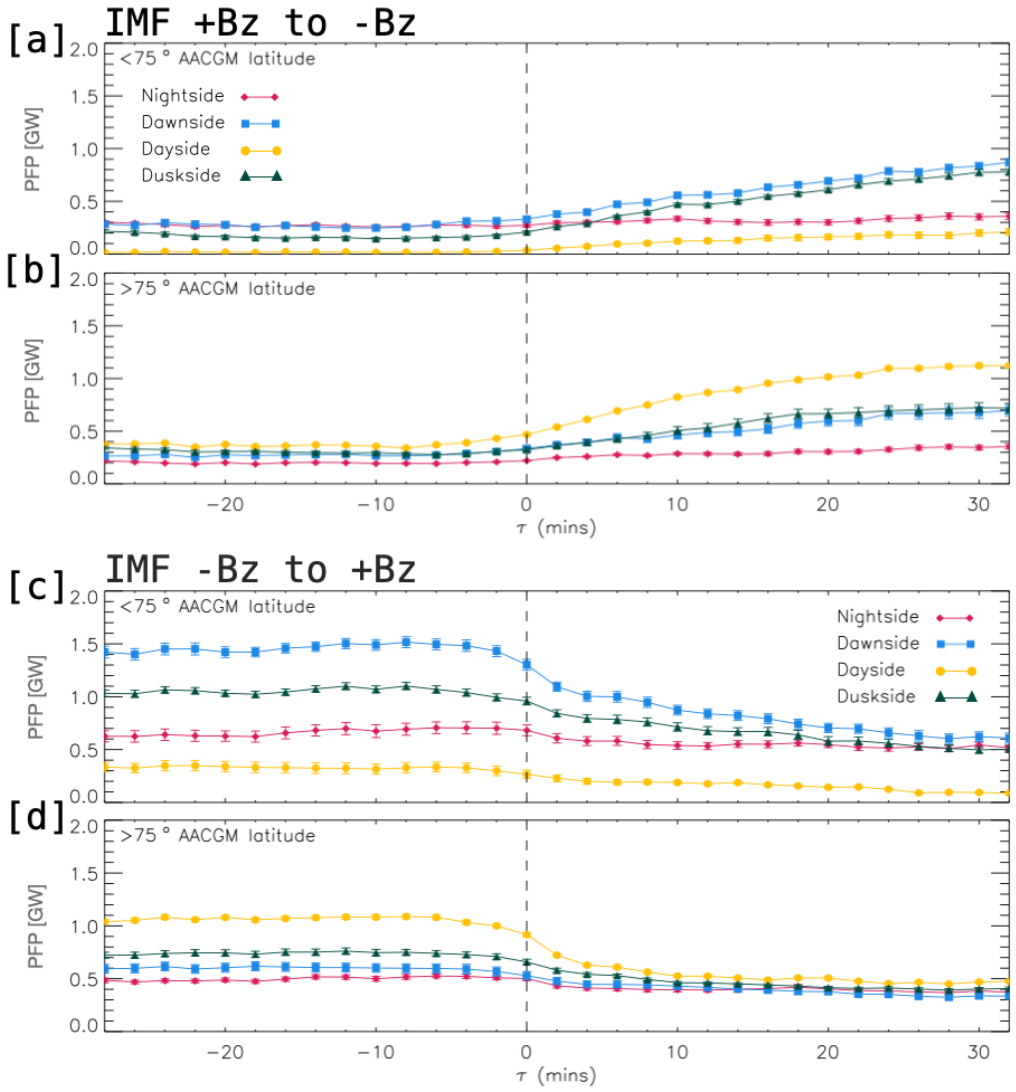


**Figure 2.** Superposed epoch time series of the downward Poynting flux averaged over nightside, dawnside, dayside and duskside local times. [a] and [b]: northward-to-southward transitions. [c] and [d]: southward-to-northward transitions. Averages are also split into below ([a] and [c]) and above ([b] and [d]) 75° latitude. Standard errors are also shown, but are often smaller than the plotting symbols used.

for the Poynting flux magnitude to stabilise to the new IMF orientation, which will be commented on further in the discussion section.

Dayside PFP is dominant at high latitudes for the $B_z$ south-to-north transition (Figure 2d), dropping from 1.05 before $t_0$ to 0.5 GW at $t_0$+30. Duskside, dawnside and nightside PFP have lower initial magnitudes of 0.7, 0.6 and 0.5 GW respectively, all decreas-

ing to ∼0.35-0.4 GW. We note that for south-to-north $B_z$ transitions (both Figure 2d and e), the initial PFP decrease after $t_0$ appears sharper at all local times than the corresponding increase in the north-to-south transition (Figure 2a and b).

From Figure 2, it is evident that different local times and latitudinal regions respond at different rates to an IMF $B_z$ transition. In Figure 3, maps of the Poynting flux percentage increase (for $B_z$ north-to-south transitions, [a]) and percentage decrease (for south-to-north transitions, [b]) from $t_0$ are shown. Epochs shown are from $t_0$+2 minutes to $t_0$+30 minutes. Only the percentage increase or decrease is shown for respective transitions because on average, the Poynting flux does not decrease for $B_z$ north-to-south transitions and vice versa. This is not strictly true for single events and localised regions where very small PF fluctuations can occur in both the positive and negative direction, irregardless of $B_z$ transition. Small localised fluctuations, defined as a $<0.1\,\mathrm{mWm^{-2}}$ increase or decrease from $t_0$, are however removed from Figure 3. Figure 3 is not to illustrate the magnitude of Poynting flux changes in certain regions, but more as an indication of the rate of Poynting flux change normalised by initial magnitudes at $t_0$

In Figure 3a, large percentage enhancements of the Poynting flux (+100% or more) within 10 minutes of the $B_z$ north-to-south transition occur on the dayside and propagate towards the nightside, mainly between 65-75° latitude and near the pole. In particular, the post-noon sector PF appears to increase the fastest. The nightside propagation continues with increasing epoch up to 30 minutes after the transition, where percentage increases from $t_0$ reach nearly +400% on the dayside in the post- and pre-noon sectors. There is a clear gradual expansion of the enhancement regions equatorward with increasing epoch, particularly on the nightside a few hours pre- and post-midnight, where there are large percentage enhancements near 60° latitude at $t_0$+30.

Within 10 minutes of a $B_z$ south-to-north transition (Figure 3b), Poynting flux percentage decreases of several tens of percent appear to occur both on the day and nightside simultaneously. This initial decrease occurs across most local times and is roughly confined to near the pole (particularly on the dayside), as well as between 65-75° latitude on the dawn and dusk sides. PF continues to decrease on the dawn and dusk sides with increasing epoch, decreasing first at lower latitudes and then later at higher latitudes. By $t_0$+30, PF decreases by as much as 80% at lower latitudes on the dawn and dusk sides have occurred.

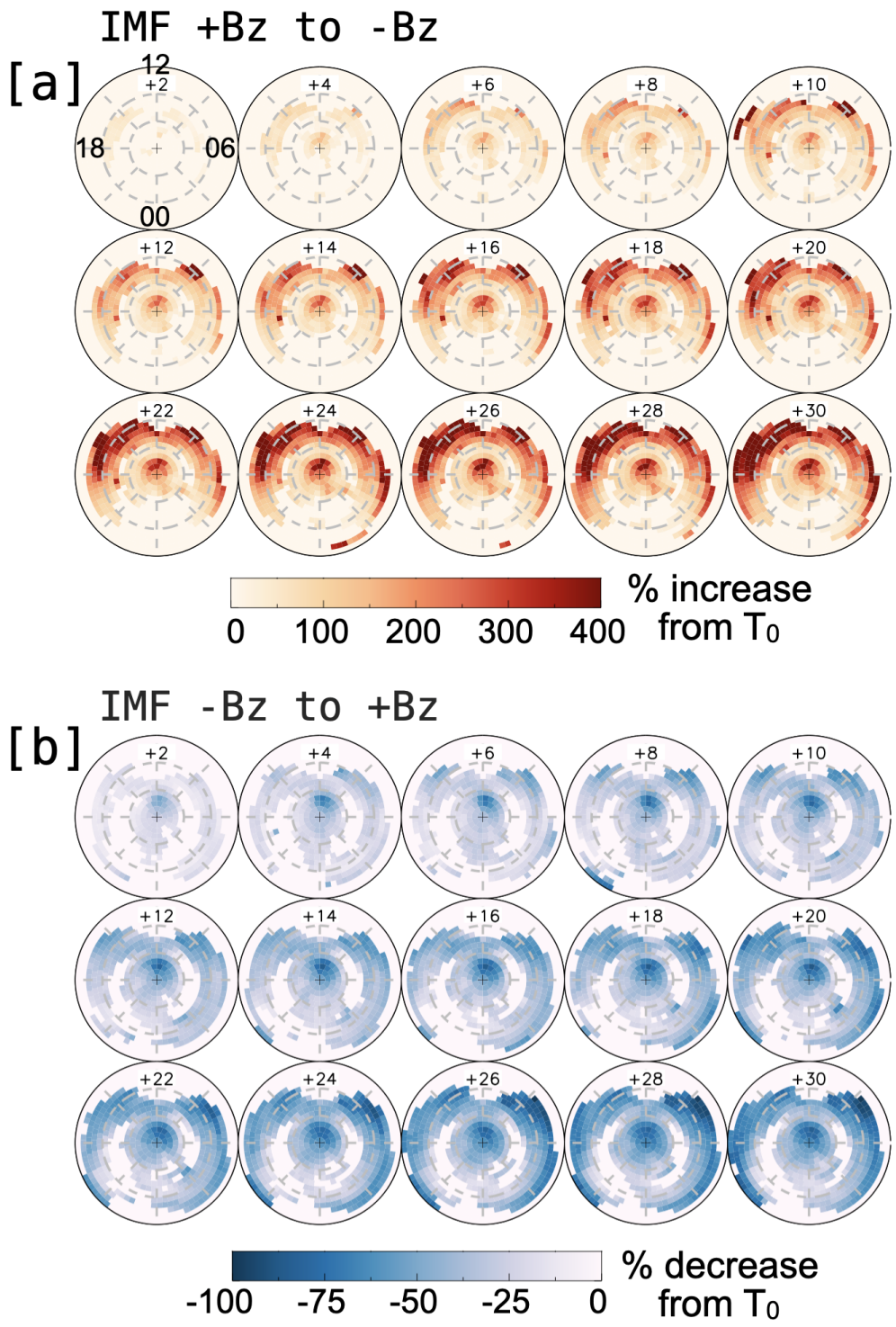


**Figure 3.** Poynting flux percentage change maps from epoch $t_0$. [a]: Percentage increase after northward-to-southward transitions. [b]: Percentage decrease after southward-to-northward transitions.

## 4 Discussion

The superposed epoch analysis presented in this study has shown the reconfiguration process of high-latitude Poynting flux in response to sign transitions of the IMF $B_z$ component, with a two-minute temporal resolution and a spatial resolution of a few hundred kilometres. The Poynting flux patterns shown in this study have a similar general morphology to those in previous studies of Poynting Flux/Joule heating (e.g. Weimer, 2005; Cosgrove et al., 2014) as well as the initial manuscript that introduces this data set (Billett et al., 2021). In short, Poynting flux is mostly dissipated at the the auroral electrojets where R1/R2 FACs close on the dawn/dusk sides, as well as around the dayside cusp at $\sim$80° latitude. Many previous authors have noted that the high-latitude ionosphere responds almost instantly to IMF changes (e.g. Murr & Hughes, 2001), and we too observe a very fast (<2 minute) response of the Poynting flux for both north-to-south and south-to-north $B_z$ transitions. The differences between the magnitude of Poynting flux before a transition and 30 minutes after are drastic, but the timescales of which changes occur in local time are gradual and not symmetric for opposite $B_z$ transitions.

We have found that 30 minutes is not long enough for the morphology of Poynting flux to fully reconfigure after an IMF transition, but is long enough to reveal significant asymmetries between the two transitions types shown here. Figure 2a and d for example shows that PFP in the low latitude dawn and dusk sectors do not totally converge to pre-transition magnitudes of the opposite transition. The full Poynting flux reconfiguration timescale is thus consistent with FAC reconfiguration timescales reported by previous authors (e.g. Anderson et al., 2018; Coxon et al., 2019). Our results are also in agreement with Moretto et al. (2021), in that most of the Poynting flux reconfigures within 30 minutes following a $B_z$ transition. The high-latitude dayside region, the area dominated by Poynting flux into the cusp, conversely appears to completely reconfigure within 30 minutes of a $B_z$ transition. As the cusp region is typically close to the boundary between open and closed (to the solar wind) geomagnetic field lines, the shorter reconfiguration time is perhaps not surprising.

For both $B_z$ transitions, there is a region close to the pole on the dayside that experiences a large percentage increase or decrease in downward Poynting flux (Figure 3). This region is on newly opened field lines following a southward transition, and connected to the magnetospheric lobes following a northward transition. The Poynting flux mag-

nitude is not particularly large near the pole compared to the main regions of enhancement, but the change that occurs there is drastic probably because the electric field rapidly changes in response to IMF orientation fluctuations. During southward IMF for example, **E** is strongly duskward near the pole (i.e. anti-sunward convection) and starts decreasing within a few minutes following a northward turning (Knipp et al., 1991). The opposite also occurs quickly for the north-to-south transition.

Evident in our analysis is the expanding-contracting polar cap (Cowley & Lockwood, 1992). After IMF $B_z$ north-to-south transitions for example, we can clearly see an immediate increase of the dayside downward Poynting flux, followed by increases at local times gradually approaching nightside local times (Figure 3a). This is in agreement with magnetopause reconnection transferring flux into the polar cap and causing it to expand, activating R1 and R2 field aligned currents on the dayside. Anderson et al. (2018) noted that night side FAC activation was lagged approximately 30 minutes after the onset of dayside currents, caused by the release of magnetic flux build up in the magnetotail, which would explain why Poynting flux increases appear heavily dayside dominant for the first 30 minutes following a $B_z$ north-to-south transition. A future study in this area could focus on Poynting flux changes later than 30 minutes post IMF transition, examining in more depth the dayside-to-nightside morphology changes.

A perhaps surprising result is that for $B_z$ south-to-north transitions, the decrease of Poynting flux at both dayside and nightside local times seem relatively symmetric (Figure 3b), with perhaps a slightly faster decrease on the dayside. It would perhaps be expected that the sudden ending of magnetopause reconnection would cause dayside Poynting flux to decrease whilst nightside reconnection lingers, causing a lagged nightside response (in line with the ∼30-minute reconfiguration times of the ionospheric electric field; Grocott & Milan, 2014). As this is not the case, the relatively symmetric decrease of Poynting flux at most local times could be due to the neutral wind flywheel effect maintaining the ionospheric electric field. That is, after the winds were previously enhanced by ion-neutral collisions (whilst the ionosphere was being actively driven by magnetopause reconnection), they maintained ionospheric plasma circulation when the IMF turned northward (e.g. Deng et al., 1991).

In addition to the ionospheric electric field, the Poynting flux is also controlled by magnetic perturbations from FACs. The role of the ionospheric Pedersen conductance

plays an important role in the generation and decay of FACs, thus impacting the decay of Poynting flux after the south-to-north $B_z$ transition. A higher conductance can result in slower FAC formation or decay (Moretto et al., 2021), so the lower conductance of the nightside compared to the dayside would result in faster nightside FAC decay. Immediately after a northward transition of $B_z$ however, following the extended period of southward $B_z$, substorms and the auroral oval may still be active and thus contribute to higher conductance in the nightside auroral zones. Additionally, on the dayside, the generation of NBZ currents following a northward IMF transition impede dayside FAC decay (Milan et al., 2018). After a $B_z$ northward transition, there must be a complicated balance between conductance at various dayside and nightside local times for the Poynting flux to decrease roughly at the same rate.

## 5 Summary

In summary, we have performed a superposed epoch analysis of the high-latitude northern hemisphere Poynting flux to changes in the IMF $B_z$ component. The analysis was carried out using ∼7.5 years of overlapping SuperDARN and AMPERE data at a 2-minute resolution, allowing for a data driven look at how the magnitude and morphology of Poynting flux changes when then Dungey cycle is switched "on" or "off". Our key results are that:

- $B_z$ positive-to-negative and negative-to-positive transitions are not symmetric in how Poynting flux increases or decreases. For positive-to-negative, there is a clear dayside-to-nightside progression of the increasing Poynting flux. For negative-to-positive transitions, Poynting flux decreases simultaneously at most local times, with dayside Poynting flux decreasing only slightly faster than that on the nightside.
- Total reconfiguration times of the Poynting flux morphology and magnitudes are longer than 30 minutes, except in the high-latitude cusp region where it is roughly 30 minutes.

It is likely that there is a complicated interplay between ionospheric conductance on the dayside and nightside, which is affecting Poynting flux decay rates for $B_z$ negative-to-positive transitions and resulting in the near simultaneous decrease at most local times. For example, lingering auroral activity on the nightside or the formation of NBZ cur-

rents on the dayside could be lengthening or shortening field-aligned current decay rates respectively. There is also a potential impact from thermospheric winds, as they could maintain the ionospheric electric field after northward $B_z$ turnings due to the flywheel effect.

**Acknowledgments**

This research was supported by the National Sciences and Engineering Research Council of Canada (NSERC). DDB was supported by NSERC CREATE Grant #479771-20, whilst KM was supported by NSERC Discovery Grant #RGPIN 05472-2017. The authors acknowledge the use of data from SuperDARN, an international project made possible by the national funding agencies of Australia, Canada, China, France, Italy, Japan, South Africa, Norway, the United Kingdom and the United States of America. SuperDARN data can be downloaded from Globus, instructions of which are provided here: `https://superdarn.ca/data-products`. SuperDARN data in this study was processed using the Radar Software Toolkit (RST), version 4.5: `https://doi.org/10.5281/zenodo.4435297`. We also thank the AMPERE team and the AMPERE Science Center for providing the Iridium derived data products, which can be plotted and downloaded at: `http://ampere.jhuapl.edu/`.

## References

Anderson, B. J., Korth, H., Waters, C. L., Green, D. L., Merkin, V. G., Barnes, R. J., & Dyrud, L. P. (2014). Development of large-scale Birkeland currents determined from the Active Magnetosphere and Planetary Electrodynamics Response Experiment. *Geophysical Research Letters*, *41*(9), 3017–3025.

Anderson, B. J., Olson, C. N., Korth, H., Barnes, R. J., Waters, C. L., & Vines, S. K. (2018). Temporal and spatial development of global Birkeland currents. *Journal of Geophysical Research: Space Physics*, *123*(6), 4785–4808.

Bhattarai, S. K., Lopez, R. E., Bruntz, R., Lyon, J. G., & Wiltberger, M. (2012). Simulation of the polar cap potential during periods with northward interplanetary magnetic field. *Journal of Geophysical Research: Space Physics*, *117*(A4).

Billett, D. D., Grocott, A., Wild, J. A., Walach, M.-T., & Kosch, M. J. (2018). Diurnal variations in global Joule heating morphology and magnitude due

to neutral winds. *Journal of Geophysical Research: Space Physics*, *123*(3), 2398–2411.

Billett, D. D., Perry, G. W., Clausen, L. B. N., Archer, W. E., McWilliams, K. A., Haaland, S., ... Anderson, B. J. (2021). The Relationship Between Large Scale Thermospheric Density Enhancements and the Spatial Distribution of Poynting Flux. *Journal of Geophysical Research: Space Physics*, e2021JA029205. doi: https://doi.org/10.1029/2021JA029205

Chisham, G., Lester, M., Milan, S. E., Freeman, M. P., Bristow, W. A., Grocott, A., ... Walker, A. D. M. (2007). A decade of the Super Dual Auroral Radar Network (SuperDARN): scientific achievements, new techniques and future directions. *Surveys in Geophysics*, *28*(1), 33-109. doi: 10.1007/s10712-007-9017-8

Cosgrove, R. B., Bahcivan, H., Chen, S., Strangeway, R. J., Ortega, J., Alhassan, M., ... others (2014). Empirical model of Poynting flux derived from FAST data and a cusp signature. *Journal of Geophysical Research: Space Physics*, *119*(1), 411–430.

Cowley, S. W. H., & Lockwood, M. (1992). Excitation and decay of solar wind-driven flows in the magnetosphere-ionosphere system. In *Annales geophysicae* (Vol. 10, pp. 103–115).

Coxon, J. C., Milan, S. E., Carter, J. A., Clausen, L. B. N., Anderson, B. J., & Korth, H. (2016). Seasonal and diurnal variations in AMPERE observations of the Birkeland currents compared to modeled results. *Journal of Geophysical Research: Space Physics*, *121*(5), 4027–4040.

Coxon, J. C., Shore, R. M., Freeman, M. P., Fear, R. C., Browett, S. D., Smith, A. W., ... Anderson, B. J. (2019). Timescales of Birkeland currents driven by the IMF. *Geophysical Research Letters*, *46*(14), 7893–7901.

Deng, W., Killeen, T. L., Burns, A. G., & Roble, R. G. (1991). The flywheel effect: Ionospheric currents after a geomagnetic storm. *Geophysical research letters*, *18*(10), 1845–1848.

Dods, J., Chapman, S. C., & Gjerloev, J. W. (2017). Characterizing the ionospheric current pattern response to southward and northward IMF turnings with dynamical SuperMAG correlation networks. *Journal of Geophysical Research: Space Physics*, *122*(2), 1883–1902.

Dungey, J. W. (1961). Interplanetary magnetic field and the auroral zones. *Physical*

*Review Letters*, *6*(2), 47.

Greenwald, R. A., Baker, K. B., Dudeney, J. R., Pinnock, M., Jones, T. B., Thomas, E. C., ... others (1995). Darn/superdarn. *Space Science Reviews*, *71*(1-4), 761–796.

Grocott, A., & Milan, S. E. (2014). The influence of IMF clock angle timescales on the morphology of ionospheric convection. *Journal of Geophysical Research: Space Physics*, *119*(7), 5861–5876.

Iijima, T., Potemra, T. A., Zanetti, L. J., & Bythrow, P. F. (1984). Large-scale Birkeland currents in the dayside polar region during strongly northward IMF: A new Birkeland current system. *Journal of Geophysical Research: Space Physics*, *89*(A9), 7441–7452.

Knipp, D. J., Matsuo, T., Kilcommons, L., Richmond, A., Anderson, B., Korth, H., ... Parrish, N. (2014). Comparison of magnetic perturbation data from LEO satellite constellations: Statistics of DMSP and AMPERE. *Space Weather*, *12*(1), 2–23.

Knipp, D. J., Richmond, A. D., Emery, B., Crooker, N. U., de La Beaujardiere, O., Evans, D., & Kroehl, H. (1991). Ionospheric convection response to changing imf direction. *Geophysical research letters*, *18*(4), 721–724.

Milan, S. E. (2009). Both solar wind-magnetosphere coupling and ring current intensity control of the size of the auroral oval. *Geophysical Research Letters*, *36*(18).

Milan, S. E., Carter, J. A., Sangha, H., Laundal, K. M., Østgaard, N., Tenfjord, P., ... others (2018). Timescales of dayside and nightside field-aligned current response to changes in solar wind-magnetosphere coupling. *Journal of Geophysical Research: Space Physics*, *123*(9), 7307–7319.

Moretto, T., Hesse, M., Kuznetsova, M., Rastätter, L., Vennerstrøm, S., & Tenfjord, P. (2021). How does the magnetosphere go to sleep? *Journal of Atmospheric and Solar-Terrestrial Physics*, 105626.

Moretto, T., Hesse, M., Vennerstrøm, S., & Tenfjord, P. (2018). Estimating the rate of cessation of magnetospheric activity in ampere field-aligned currents. *Geophysical Research Letters*, *45*(23), 12–713.

Murr, D. L., & Hughes, W. J. (2001). Reconfiguration timescales of ionospheric convection. *Geophysical Research Letters*, *28*(11), 2145–2148.

Nishitani, N., Ruohoniemi, J. M., Lester, M., Benjamin, J., Baker, H., Koustov, A. V., ... Kikuchi, T. (2019). Review of the accomplishments of mid-latitude Super Dual Auroral Radar Network (SuperDARN) HF radars. *Progress in Earth and Planetary Science*, *6*(1). doi: 10.1186/s40645-019-0270-5

Onsager, T. G., Scudder, J. D., Lockwood, M., & Russell, C. T. (2001). Reconnection at the high-latitude magnetopause during northward interplanetary magnetic field conditions. *Journal of Geophysical Research: Space Physics*, *106*(A11), 25467–25488.

Ruohoniemi, J. M., & Baker, K. B. (1998). Large-scale imaging of high-latitude convection with Super Dual Auroral Radar Network HF radar observations. *Journal of Geophysical Research: Space Physics*, *103*(A9), 20797–20811.

Shepherd, S. G. (2014). Altitude-adjusted corrected geomagnetic coordinates: Definition and functional approximations. *Journal of Geophysical Research: Space Physics*, *119*(9), 7501–7521.

Snekvik, K., Østgaard, N., Tenfjord, P., Reistad, J. P., Laundal, K. M., Milan, S. E., & Haaland, S. E. (2017). Dayside and nightside magnetic field responses at 780 km altitude to dayside reconnection. *Journal of Geophysical Research: Space Physics*, *122*(2), 1670–1689.

Waters, C. L., Anderson, B. J., Greenwald, R. A., Barnes, R. J., & Ruohoniemi, J. M. (2004). High-latitude poynting flux from combined Iridium and SuperDARN data. In *Annales geophysicae* (Vol. 22, pp. 2861–2875).

Weimer, D. R. (2005). Improved ionospheric electrodynamic models and application to calculating Joule heating rates. *Journal of Geophysical Research: Space Physics*, *110*(A5).

Yu, Y., & Ridley, A. J. (2009). Response of the magnetosphere-ionosphere system to a sudden southward turning of interplanetary magnetic field. *Journal of Geophysical Research: Space Physics*, *114*(A3).